Electronic and photophysical properties of a heterometallic Ru(II)–Cu(I) Kuratowski complex: insights from spectroscopy and density functional theory calculations

Wiebke G. Rehfuß, Andreas Kalytta-Mewes, Maryana Kraft, Dirk Volkmer

Angaben zur Veröffentlichung / Publication details:

Rehfuß, Wiebke G., Andreas Kalytta-Mewes, Maryana Kraft, and Dirk Volkmer. 2025. "Electronic and photophysical properties of a heterometallic Ru(II)–Cu(I) Kuratowski complex: insights from spectroscopy and density functional theory calculations." European Journal of Inorganic Chemistry 28 (22): e202500190. https://doi.org/10.1002/ejic.202500190.

EurJIC
European Journal of Inorganic Chemistry

Research Article
doi.org/10.1002/ejic.202500190

Chemistry Europe
European Chemical Societies Publishing

www.eurjic.org

Electronic and Photophysical Properties of a Heterometallic Ru(II)–Cu(I) Kuratowski Complex: Insights from Spectroscopy and Density Functional Theory Calculations

Wiebke G. Rehfuß, Andreas Kalytta-Mewes, Maryana Kraft, and Dirk Volkmer*

Polynuclear metal complexes offer tunable electronic properties that are valuable for photocatalysis and molecular electronics. Herein, the synthesis and characterization of a poly-heteronuclear Kuratowski complex, $[Ru^{II}Cu^{I}_4(Me_2bta)_6(PPh_3)_4]$ is presented. This complex is designed to investigate the electronic coupling between strongly reducing Cu(I) centers and a Ru(II) ion, mediated by a highly symmetric framework of triazolate ligands. Electrochemical studies reveal coupled redox behavior between Ru(II) and Cu(I), while UV–vis spectroscopy shows an overlapping Ru- and Cu-centered metal-to-ligand charge transfer (MLCT) band, redshifted in comparison to its $\{Ru^{II}Zn^{II}_4\}$ analog. Despite this, fluorescence lifetime measurements indicate that ultrafast nonradiative relaxation limits electron transfer between the metal centers. Density functional theory (DFT) and time-dependent-DFT calculations confirm that ligand-field effects, rather than direct Ru–Cu interactions, drive the MLCT redshift. These observations offer tentative insights into excited-state dynamics and highlight design aspects for controlling electronic communication in polynuclear systems.

1. Introduction

Photocatalysts capable of multielectron redox processes are of particular interest in areas such as artificial photosynthesis and organic synthesis, as they enable stepwise electron and hole transfer. This improves charge separation and enhances catalytic efficiency.[1] Polynuclear metal complexes are promising candidates for such applications, as they offer tunable electronic interactions between multiple metal centers.[2] By incorporating multiple light-absorbing and redox-active sites, these systems can facilitate sequential electron transfer and stabilize reactive intermediates, potentially leading to more efficient and selective catalytic processes.[3]

Our group has coined the term Kuratowski complexes for a unique family of homo- or heteronuclear metal complexes with a topology corresponding to the nonplanar graph $K_{3,3}$.[4,5a,b,6–8] A key advancement in the synthesis of these polynuclear complexes is the development of a versatile Ru(II) precursor complex $[Ru(Me_2bta)_2(Me_2btaH)_4]$, in which Ru(II) serves as the central metal ion, coordinated by the middle (N^2) nitrogen of six 1,2,3-benzotriazolate ligands, as shown in **Scheme 1**.[7] This complex provides an ideal template for heteronuclear Kuratowski complexes, offering four peripheral coordination sites that can be selectively occupied by metal ions other than Ru(II). Each site is formed by three external (N^1 or N^3) nitrogen atoms from μ_3-bridging 1,2,3-triazolates. Depending on the charge and coordination preferences of the added metal ions, these positions can be completed by either neutral ligands (e.g., for monovalent ions) or anionic ligands such as halides or pseudohalides (for divalent ions).

Recently, a series of heteronuclear Kuratowski complexes incorporating redox-active 3 d metal ions has been reported, exhibiting intriguing electronic and photophysical properties.[4,7,9] These studies demonstrated a pronounced influence of the peripheral heterometal ions on the electron distribution around the Ru(II) center.[8] Building on this foundation, our present work investigates the potential of such complexes to undergo multielectron transfer processes. Specifically, we aim to evaluate whether the cascading redox properties of the system enable electron transfer between photoexcited Ru(II), the benzotriazolate ligands, and an electron-rich heterometal.

Therefore, we expand the scope of heteronuclear Kuratowski complexes by introducing Cu(I) ions into the peripheral positions of a Ru(II)-centered framework. As a Cu(I) precursor, we selected $[Cu(MeCN)_2(PPh_3)_2][BF_4]$, inspired by previous reports on structurally similar "reverse-umbrella-like" Cu(I)-1,2,3-triazole compounds.[10] The presence of PPh_3 ligands stabilizes the Cu(I) oxidation state against disproportionation and improves solubility in organic solvents, facilitating both synthesis and characterization.

2. Results and Discussion

This work outlines the successful synthesis of the heteronuclear Kuratowski complex $[Ru^{II}Cu^{I}_4(Me_2bta)_6(PPh_3)_4]$ (compound 1).

W. G. Rehfuß, A. Kalytta-Mewes, M. Kraft, D. Volkmer
Chair of Solid State and Materials Chemistry
Institute of Physics
University of Augsburg
Universitaetsstrasse 1, D-86159 Augsburg, Germany
E-mail: dirk.volkmer@physik.uni-augsburg.de

Supporting information for this article is available on the WWW under https://doi.org/10.1002/ejic.202500190

Research Article
doi.org/10.1002/ejic.202500190

Chemistry Europe
European Chemical Societies Publishing

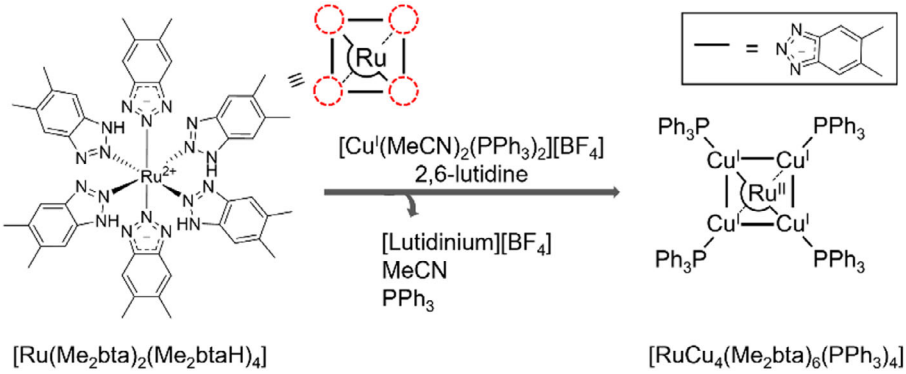

Scheme 1. Synthesis of compound 1. Reaction of the ruthenium precursor complex [Ru(Me$_2$bta)$_2$(Me$_2$btaH)$_4$] with four equivalents of [Cu(MeCN)$_2$(PPh$_3$)$_2$][BF$_4$] and 2,6-lutidine in trichloromethane for 3 days at room temperature.

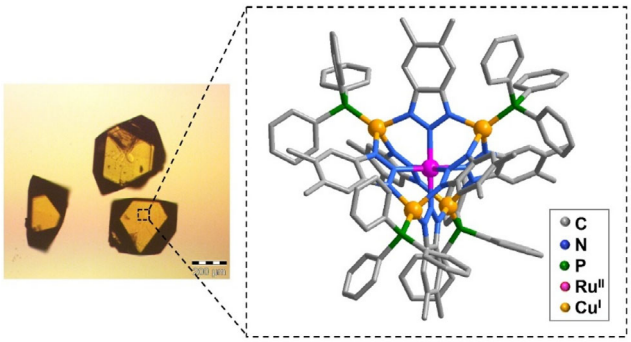

Figure 1. Left: Optical microscope image of compound 1; right: Ball and stick representation of compound 1.

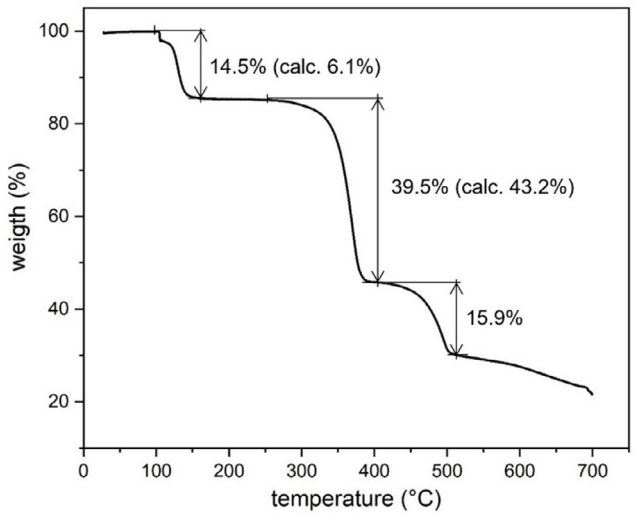

Figure 2. TGA curve of compound 1, measured in N_2 with a heating rate of 10 K min^{-1}.

The synthetic process involves the preparation of a copper(I) precursor complex, [Cu(MeCN)$_2$(PPh$_3$)$_2$][BF$_4$], employing an established procedure found in literature.[10] This precursor was subsequently reacted with [Ru(Me$_2$bta)$_2$(Me$_2$btaH)$_4$] in chloroform in the presence of 2,6-lutidine as an auxiliary base to ensure complete deprotonation of the benzotriazole ligands. Upon addition of diethyl ether to the resulting clear yellow solution, slow evaporation at room temperature afforded well-defined yellow prismatic crystals of compound 1 (yield: 72%), as displayed in **Figure 1**.

Compound 1 was characterized through multiple analytical techniques, including single-crystal X-ray diffraction (XRD), thermogravimetric analysis (TGA), Fourier-transform infrared (FT-IR) and Raman spectroscopy, inductively coupled plasma optical emission spectroscopy (ICP-OES), and elemental analysis (CHN). Phase purity of compound 1 was confirmed by powder XRD (PXRD) under ambient conditions, with the experimental pattern matching the simulated data from single-crystal analysis (Figure S1, Supporting Information). The crystal structure revealed a significant inclusion of diethyl ether molecules, which remained within the lattice even after several days of air exposure. This observation prompted further investigation into the thermal stability of the compound. TGA was performed in a nitrogen atmosphere with a heat rate of 10 K min^{-1}, as shown in **Figure 2**. Compound 1 exhibits a significant mass loss starting at 100 °C, corresponding to the removal of occluded solvent molecules and amounting to 14.5%. The calculated mass loss for the modeled diethyl ether molecules is 6.1%, suggesting the presence of additional, possibly disordered or partially occupied, solvent molecules within the structure. This interpretation is further supported by a porosity analysis using Mercury,[11] which indicates that the accessible voids in the crystal lattice could theoretically accommodate up to 14 diethyl ether molecules per complex unit.

Additionally, the temperature at which this mass loss occurs exceeds the boiling point of liquid diethyl ether by 65 °C, demonstrating a strong occlusion of diethyl ether molecules in the crystal packing arrangement of the complexes. Above 300 °C, a second defined mass loss is observed. This mass loss of 39.5% can be attributed to the neutral PPh$_3$ ligands leaving the structure (calc. 43.2%). Here, the mass loss starts at temperatures well below the boiling point of PPh$_3$ (377 °C), indicating weak coordination of the phosphine ligands to the Cu(I) centers. This implies that, in solution, ligand exchange with less sterically demanding donors may be feasible, potentially expanding the compound's applicability. Further studies are needed, as the possible presence of trigonal-pyramidal Cu(I) centers could be highly relevant for small-molecule activation.[12] The last mass loss step starts at a

Research Article
doi.org/10.1002/ejic.202500190

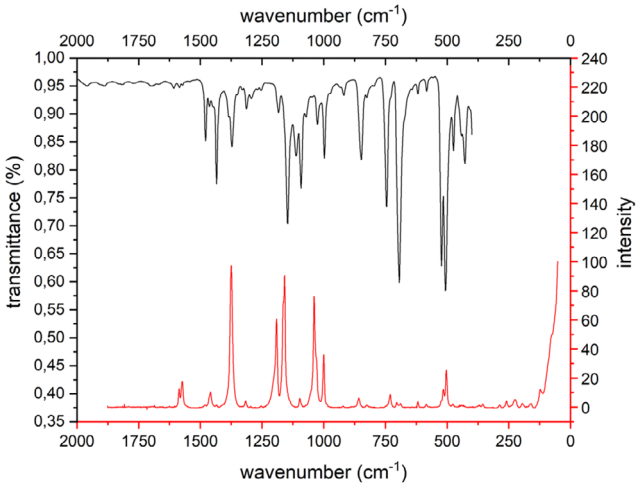

Figure 3. FT-IR and Raman plots of compound 1.

temperature above 400 °C, whereby the decomposition of the complex continues.

The IR and Raman spectra of the Ru(II)-Cu(I) heteronuclear complex exhibit a large number of vibrational bands due to the structural complexity of the system, as shown in **Figure 3**. The full FT-IR plot is shown in Figure S2, Supporting Information. To aid interpretation, selected key vibrational bands from both spectra are listed in **Table 1** along with tentative mode assignments based on characteristic group frequencies and comparison to literature data.

In the IR spectrum, weak bands in the 3050–2850 cm^{-1} range are attributed to C—H stretching modes of aromatic and aliphatic groups. Strong bands in the fingerprint region (1600–1000 cm^{-1}) are consistent with C═C and C—N stretching vibrations from the aromatic ligands, particularly the benzotriazole and phenyl rings. The P—C stretching modes of the triphenylphosphine ligands appear between 1100 and 900 cm^{-1}, with signals at 1091, 1025, and 997 cm^{-1}. Bands observed in the lower-frequency region (600–400 cm^{-1}) are assigned to M—N and M—P (Ru—N, Cu—N, Cu—P) stretching vibrations, with prominent peaks at 522, 505, and 474 cm^{-1}.

The Raman spectrum complements the IR data and is dominated by a strong band at 1374 cm^{-1}, attributed to C—N and C—C stretching and ring deformation modes of the benzotriazole ligands. Additional strong bands are observed at 1191, 1158, and 1039 cm^{-1} likely arising from coupled C—N stretches and ring deformations of both benzotriazole and phenyl rings. Weaker bands in the 1000–850 cm^{-1} range may originate from ring breathing modes; minor P—C stretching contributions from the triphenylphosphine ligands are also possible in this region, though not prominent. Weak features below 600 cm^{-1} are assigned to metal–ligand vibrations involving Ru—N, Cu—N, and Cu—P stretching.[13]

3. Crystallographic Studies

A single-crystal XRD (SCXRD) analysis reveals that compound 1 crystallizes in the monoclinic crystal system, space group $P2_1$ (no. 4), which corresponds to the C_2 point group. This deviates from the more commonly observed tetragonal crystal system found in related Kuratowski complexes.[4,6,9,14] The deviation arises from the structural disorder in two out of the twelve phenyl groups of the coordinated PPh_3 ligands, which affects the overall packing arrangement. **Figure 4**a displays a ball-and-stick model of compound 1, emphasizing the positional disorder observed in two of the phenyl rings of the triphenylphosphine (PPh_3) ligands. Figure 4b illustrates the tetrahedral coordination environment around the Cu(I) center, which is coordinated by three triazolate ligands and one PPh_3 ligand. Furthermore, Figure 4c presents a projection along one of the threefold symmetry axes passing through the P···Cu···Ru atoms, where Cu and P are obscured behind Ru, leaving only the coordinating ligands visible. Detailed crystallographic data are presented in Table S1, Supporting Information. All identifiable solvent molecules were included in the crystallographic model based on distinct residual electron density peaks and refined with anisotropic displacement parameters where applicable.

The central ruthenium ion in compound 1 is octahedrally coordinated by six central nitrogen atoms (N^2) from 1,2,3-triazolate ligands, with bond lengths ranging from 2.125 to 2.135 Å. Compared to $[RuZn_4Cl_4(Me_2bta)_6]$ (which exhibits a single Ru—N bond length of 2.116 Å), the octahedral coordination sphere in compound 1 is only slightly distorted.[4] Similarly, the average Ru—N bond length in compound 1 is slightly longer than in $[Ru(bipy)_3]^{2+}$ (2.053 Å), suggesting a weaker π-backbonding interaction with the 1,2,3-benzotriazolate ligands.[15] The

Table 1. Selected vibrational bands observed in the FT-IR and Raman spectra of compound 1 with tentative mode assignments. Bands were assigned based on characteristic group frequencies and comparison to literature data.

Wavenumber [cm^{-1}]	Assignment	IR/Raman	Intensity
3052–2852	C—H stretching (aromatic/aliphatic)	IR	weak
1479, 1434, 1373	C═C/C—N stretching (benzotriazole, phenyl)	IR	medium–strong
1374, 1191, 1158	C—N/ring deformation (benzotriazole)	Raman	strong
1091, 1025, 997	P—C stretching (PPh_3)	IR	strong
999, 855, 731	Ring breathing modes (phenyl, benzotriazole)	Raman	strong/weak
584, 522, 505, 474	M—N/M–P stretching (Ru—N, Cu—N, Cu—P)	IR	medium–strong
516, 503	Metal–ligand modes	Raman	weak–medium
221, 120	Lattice/coordination modes	Raman	weak

Research Article
doi.org/10.1002/ejic.202500190

Chemistry Europe
European Chemical Societies Publishing

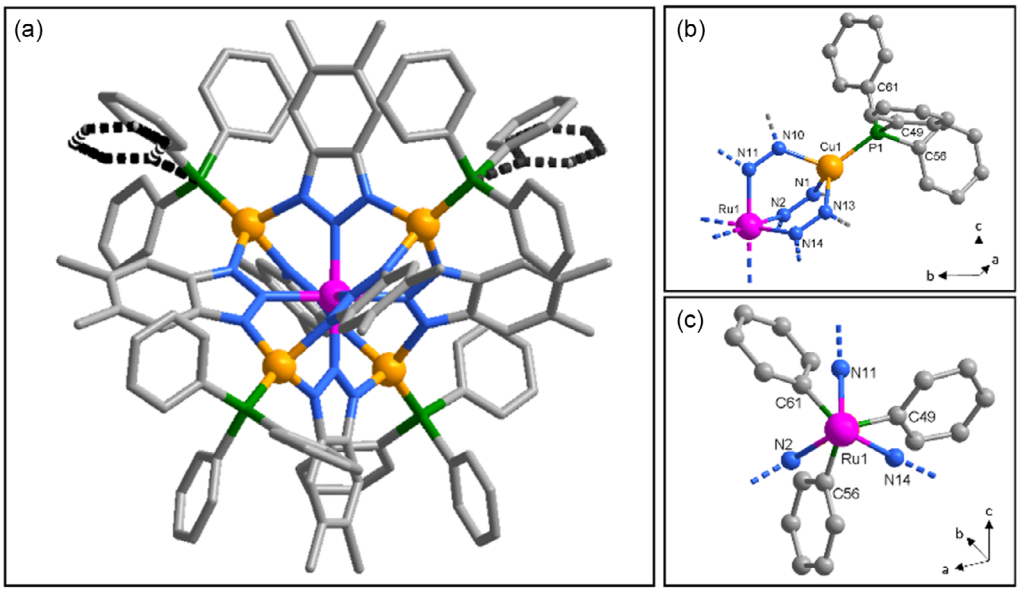

Figure 4. a) Molecular structure of compound 1 showing positional disorder two phenyl groups of PPh_3. Hydrogen atoms are omitted for clarity. b) Local coordination environment of the Cu(I) centers, displaying a distorted tetrahedral geometry involving three triazolate and one PPh_3 ligand. c) Projection along one of the tridentate axes passing through the atoms P···Cu···Ru.

N—Ru—N valence angles in compound 1 vary minimally from the ideal 90° and 180°, with deviations of up to 0.6°, which is comparable to the nearly ideal octahedral geometries observed in other Kuratowski complexes.[4,9]

The external nitrogen atoms (N^1 and N^3) of the 1,2,3-benzotriazolate ligands coordinate four different copper(I) -centers-, each further coordinated by a PPh_3 side ligand. The Cu—N bond lengths range from 2.007 to 2.055 Å, while the Cu—P bond lengths fall between 2.166 and 2.170 Å. These bond lengths are nearly identical to those in the homonuclear structure $[Cu_5(bta)_6(PPh_3)_4]$ (bta = 1,2,3-benzotriazolate).[16]

Despite this lower crystallographic symmetry in the solid state, density functional theory (DFT) calculations suggest that the most energetically favorable gas-phase structure of compound 1 adopts an S_4 symmetric geometry. In the idealized case, the highest possible symmetry for this complex would be T_d, as observed for other $[M_5X_4(bta)_6]$ complexes.[9] However, achieving T_d symmetry would require perfect alignment of the PPh_3 phenyl groups along the local C_3 axes, which is sterically hindered by hydrogen atoms on the phenyl rings. Instead, the system relaxes into an S_4 symmetric geometry, where the phenyl groups are no longer symmetry-equivalent.

The reduction in symmetry is also evident in the molecular geometry obtained from the crystal structure. The Cu···Cu nonbonding distances show slight deviations from ideal tetrahedral symmetry. Notably, the opposing Cu(2)···Cu(3) and Cu(1)···Cu(4) edges are slightly elongated (5.979 and 5.982 Å), defining a pseudo-S_4 axis in line with the gas-phase structure. The remaining Cu···Cu distances (5.924–5.936 Å) support a nearly symmetric but slightly distorted configuration. These geometric features are illustrated in **Figure 5**. Overall, the data suggest that although crystal packing lowers the symmetry in the solid state, the intrinsic molecular geometry in the gas phase closely approaches S_4 symmetry, largely influenced by steric hindrance from the PPh_3 ligands.

4. Cyclic Voltammetry (CV)

The electrochemical behavior of compound 1 was investigated by CV. Voltammograms recorded at a scan rate of 20 mV s^{-1} are shown in **Figure 6**, with additional data at varying scan rates provided in Figure S3 and S4, Supporting Information. Measurements were performed in trichloromethane ($CHCl_3$) with 0.1 M $[NBu_4][PF_6]$ as supporting electrolyte and a complex concentration of 0.5 mM.

CV revealed an unexpected redox response for the Ru(II/III) couple. Upon scanning up to 1.15 V versus $DmFc^+$/DmFc, a single-electron reversible oxidation wave (I^{Ox}) is observed at ${}^{I}E^{ox}_{1/2} = 0.42$ V versus $DmFc^+$/DmFc, corresponding to the Ru(II/III) oxidation (Figure 6b). However, when the scan is extended to 1.65 V versus $DmFc^+$/DmFc, a notable transformation occurs. As depicted in Figure 6a, the reversible oxidation wave for Ru(II/III) becomes a single-electron- irreversible oxidation wave. Additionally, a new irreversible oxidation wave appears at ${}^{I}E^{ox}_{p/2} = 1.53$ V versus $DmFc^+$/DmFc, which is assigned to the Cu(I/II) oxidation.

For comparison, Kuratowski-type complexes bearing Zn(II) or Cu(II) in the peripheral positions exhibit significantly lower Ru(II/III) oxidation potentials at 0.18 and 0.15 V versus Fc^+/Fc, respectively.[8] In contrast, incorporation of Cu(I) leads to a significantly higher Ru(II/III) oxidation potential, suggesting that Cu(I) exerts an electron-withdrawing effect on the Ru(II) center, possibly via the conjugated benzotriazolate bridges. This is a surprising result, as Cu(I), being a closed-shell d^{10} metal, is generally expected to act as an electron donor. However, π-conjugation and partial electron density transfer from Ru(II) to Cu(I) likely stabilize the highest

Research Article
doi.org/10.1002/ejic.202500190

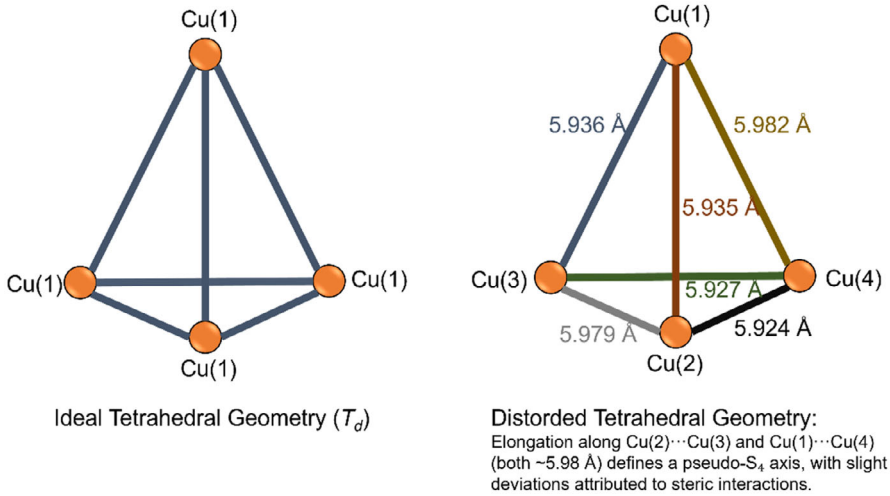

Figure 5. Comparison of an ideal tetrahedral $Cu(I)_4$ arrangement (left) with the distorted geometry observed in compound 1 (right). While the ideal T_d features six equivalent Cu···Cu edges, the experimentally determined structure exhibits slight elongation along the Cu(1)···Cu(4) and Cu(2)···Cu(3) diagonals (both ≈5.98 Å). These define a pseudo-S_4 axis, indicating a symmetry reduction from T_d due to steric effects imposed by the PPh_3 ligands.

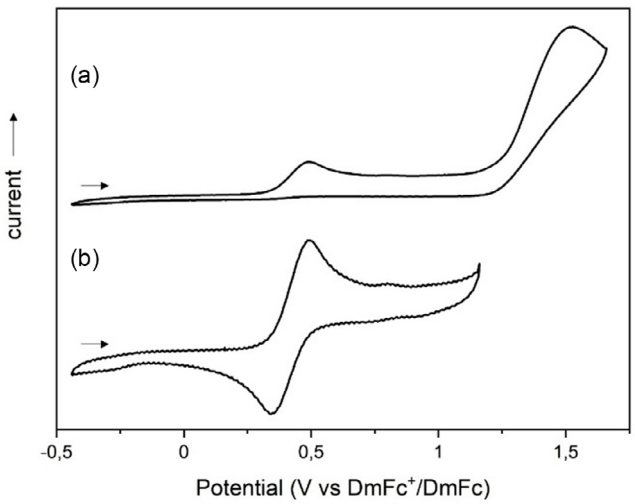

Figure 6. Cyclic voltammogram of compound 1, at a glassy carbon electrode in 0.1 M $[NBu_4][PF_6]/CHCl_3$ solution and with Ag/Ag^+ as the reference electrode. Scan rate: 20 mV s^{-1}, complex concentration: 0.5 mM. a) Potential window of −0.45 to 1.65 V versus $DmFc^+/DmFc$ b) potential window of −0.45 to 1.15 V versus $DmFc^+/DmFc$.

occupied molecular orbital (HOMO) of the Ru(II) center, resulting in the observed anodic shift.

The Cu(I/II) oxidation at ${}^{I}E^{ox}_{p/2} = 1.53$ V versus $DmFc^+/DmFc$ is consistent with values reported for Cu(I) complexes featuring similar tridentate ligand environments and PPh_3 coligands, such as $[HB(3,5\text{-}(CH_3)_2Pz)_3]CuPPh_3$ and $[HB(3,5\text{-}(CF_3)_2Pz)_3]CuPPh_3$, which exhibit similarly high oxidation potentials (1.0–1.5 V).[17] Notably, no corresponding reduction wave is detected for Cu(II), suggesting that the oxidized Cu(II) species is electrochemically unstable under the experimental conditions. This behavior likely results from ligand reorganization or structural rearrangement in $CHCl_3$, forming a species that cannot be reduced within the accessible potential window. Such irreversible electrochemical behavior is consistent with observations in related $\{Ru^{II}Cu^{II}_4\}$ Kuratowski complexes, where no reduction waves were detected under similar conditions.[8]

5. Photophysical Properties and Computational Studies

The optical absorption properties of compound 1 were investigated experimentally in trichloromethane solution at room temperature and complemented by quantum mechanical calculations. The UV–vis absorption spectrum exhibits two prominent bands at 300 and 360 nm, as shown in **Figure 7**.

The absorption band at 300 nm is attributed to intraligand $\pi \rightarrow \pi^*$ transitions, localized on both the $[Me_2bta]$ and PPh_3 ligands.

The absorption band at 360 nm, assigned to a metal-to-ligand charge transfer (MLCT) transition, likely arises from overlapping contributions involving Ru(II) and Cu(I). A comparison with related Kuratowski-type complexes further supports this assignment: the $\{Ru^{II}Zn^{II}_4\}$ complex $[Ru^{II}Zn^{II}_4(Me_2bta)_6(Tp^*)_4]$ exhibits an MLCT band at 345 nm,[8] while the homometallic $\{Cu^{II}Cu^{I}_4\}$ complex $[Cu^{II}Cu^{I}_4(bta)_6(PPh_3)_4]$ shows an MLCT absorption at 366 nm, previously attributed to Cu(I) → benzotriazolate transitions.[10]

The 15 nm redshift of the MLCT band in compound 1 relative to $\{Ru^{II}Zn^{II}_4\}$ can be attributed to the presence of PPh_3 ligands, which serve as low-energy charge-accepting orbitals. Unlike $\{Ru^{II}Zn^{II}_4\}$, which lacks PPh_3 ligands, compound 1 facilitates a Ru(II) → PPh_3 MLCT transition, confirmed by time-dependent-DFT (TD-DFT) calculations, as discussed below. Since the PPh_3 orbitals lie at lower energies compared to the benzotriazolate π-system, they induce a red shift in the MLCT absorption band.

To elucidate the electronic properties underlying these observations, DFT calculations were performed using the TURBOMOLE program package (rev. V7-8-1) with the B3-LYP functional,[18] the Karlsruhe def2-triple-zeta valence with polarization (TZVP) basis set, and Grimme's D4 dispersion correction.[19] Geometry optimizations under different symmetry constraints

Research Article
doi.org/10.1002/ejic.202500190

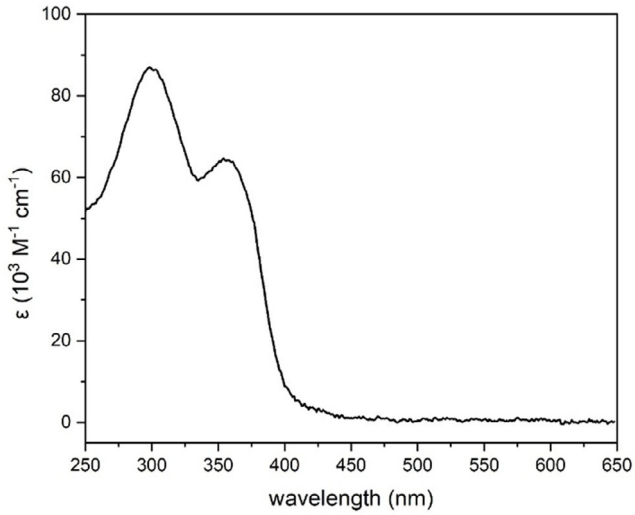

Figure 7. UV–vis absorption spectra of compound 1, recorded in $CHCl_3$ solution at room temperature. The molar extinction coefficient was determined from a concentration series (1–15 μM) using the Lambert–Beer law.

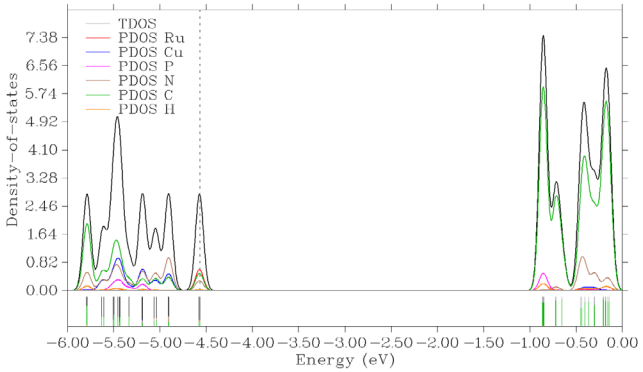

Figure 9. Projected DOS illustrating the contributions of different atomic centers to the frontier orbitals. The DOS plot highlights the localization of occupied orbitals on the Ru center and the predominant contribution of the triphenylphosphine ligands to the unoccupied states.

(T, D_2, and S_4 point groups) identified S_4 symmetry as the most stable configuration.

The calculated HOMO-lowest unoccupied molecular orbital (LUMO) gap of 3.703 eV is in fair agreement with the observed UV–vis absorption spectrum showing the onset of light absorption at a wavelength of about 400 nm (= 3.1 eV). (A slight overestimation of the HOMO-LUMO gap is frequently observed for calculations employing the B3-LYP functional) Frontier orbital analysis reveal three doubly occupied, nearly degenerate orbitals (HOMO, HOMO-1, and HOMO-2) with energies between–4.5698 and –4.5784 eV, respectively. These orbitals are strongly localized on the Ru atom, as seen in **Figure 8**a. The unoccupied frontier orbitals (LUMO to LUMO + 7), ranging from –0.8668 to –0.8487 eV, are largely delocalized across the triphenylphosphine ligands, as illustrated in Figure 8b. The density of states (DOS) function, shown in **Figure 9**, further highlights the element-specific contributions to these orbitals.

TD-DFT calculations simulated the UV–vis spectrum, using the same parameters as the ground-state calculations. Transition energies for 25 vertical singlet excitations were calculated within the random phase approximation, incorporating S_4 symmetry. The resulting broadened line spectrum, shown in Figure S5, Supporting Information, indicates that the calculated transitions are primarily intraligand in nature, as $d \rightarrow d$ transitions are forbidden.

The computational results suggest that UV irradiation could induce an MLCT transition, transferring an electron from a t_{2g}-type Ru 4 d orbital to a low-energy unoccupied orbital localized on the triphenylphosphine ligands.

While the calculated singlet-to-singlet electronic transitions reproduce ligand-centered features of the experimental spectra reasonably well, the assignment of electron transfer pathways involving MLCT transitions should be interpreted with caution. This is due to known limitations of TD-DFT, particularly when using global hybrid functionals such as B3-LYP, suffering from incorrect asymptotic behavior, which often leads to inaccurate descriptions of electron density in the outer regions of molecules. Moreover, CT processes require an appropriate treatment of

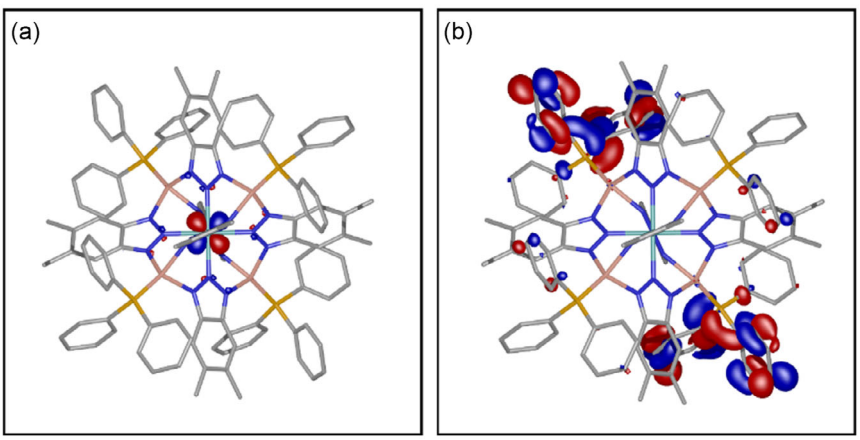

Figure 8. Frontier molecular orbitals of compound 1 calculated using DFT. a) Isosurface representation of a single HOMO (out of three nearly degenerate HOMOs which are strongly localized on the Ru center. b) Isosurface representation of a single LUMO. (LUMO to LUMO + 7 are strongly delocalized across the triphenylphosphine ligands.

Research Article
doi.org/10.1002/ejic.202500190

nonlocal electron correlation, which is only partly covered by the admixing of Fock exchange. Both inherent limitations may inaccurately predict the energies and ordering of C-T states. Combining Fock-exchange with (semi)local xc functional components via range-separation that splits the Coulomb interaction into long- and short-range components captures the physics of screening much better, and therefore is intrinsically better suited for describing CT.[20] However, while range-separated hybrid functionals can solve many deficiencies of the global hybrid functionals for simple organic molecules, their applicability for large, hetero-transition metal complexes remains computationally demanding and insufficiently benchmarked. Therefore, a comprehensive functional comparison is beyond the scope of this study.

Steady-state fluorescence measurements were conducted in oxygen-free trichloromethane solution. Although excitation of the intraligand absorption bands does not yield any observable emission, excitation of the MLCT band results in a weak emission signal characterized by a peak at 420 nm and a shoulder around 490 nm. As depicted in **Figure 10**, the emission spectrum exhibits noticeable noise, which is due to the inherently low intensity of the emitted light. Consequently, determining the fluorescence quantum yield proved challenging. The quantum yield was measured relative to anthracene ($\Phi = 0.33$), but the emission of compound 1 was found to be below the detection threshold for accurate quantification, corresponding to a quantum yield of $< 0.1\%$. Furthermore, lifetime measurements were conducted using a pulsed laser at 350 nm. In this context, compound 1 exhibits a short lifetime of 2.76 ns, a duration too short to anticipate electron transfer processes at room temperature in solution. The lifetime measurement is shown in Figure S6, Supporting Information.

The weak fluorescence of compound 1 in solution can be attributed to excited-state charge redistribution between the Ru(II) center and PPh_3 ligands upon excitation. TD-DFT calculations suggest that the lowest-energy MLCT transition involves electron transfer from the Ru(II) center to the PPh_3 ligand, which provides the LUMOs of the complex. This excitation results in the formation of a transient Ru(III)/PPh_3($\bullet^-$) charge-separated state. The CV measurements further support this assignment, as the first oxidation is observed at the Ru(II) center rather than at the Cu(I) centers.

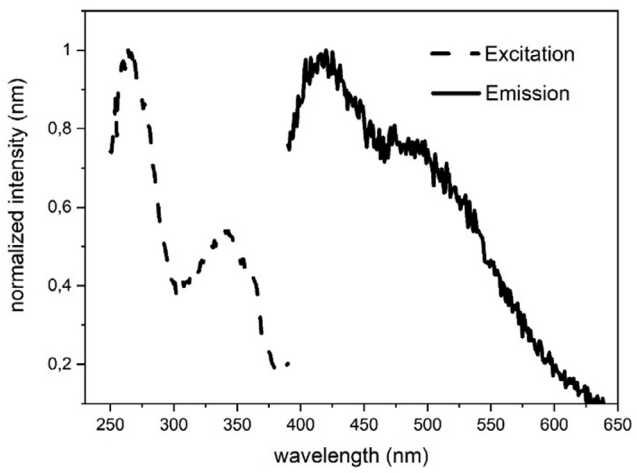

Figure 10. Fluorescence excitation (- -) and emission (–) spectra of compound 1 recorded in $CHCl_3$ solution at room temperature.

A likely mechanism for fluorescence quenching involves sequential electron transfer, where Cu(I) donates an electron to the oxidized Ru(III) center, forming a Cu(II)/PPh_3($\bullet^-$) charge-separated state. This state undergoes rapid internal electron exchange, leading to efficient non-radiative relaxation. The absence of detectable emission from this state suggests that it relaxes extremely fast via internal conversion pathways, thereby explaining the very low fluorescence quantum yield of the complex.

Future investigations could focus on designing related polynuclear complexes with coligands that stabilize the charge-separated state via $S_1 \rightarrow T_1$ intersystem crossing (ISC), potentially leading to longer-lived excited states that could be utilized for photochemical applications.

To contextualize the photophysical behavior of compound 1, it is instructive to compare it with well-known Ru(II) complexes featuring long-lived MLCT states. A classical example is $[Ru(bpy)_3]^{2+}$, which displays microsecond-range phosphorescence from a triplet MLCT state (^{3}MLCT). In such systems, rapid ISC to the ^{3}MLCT state occurs within femtoseconds, and radiative decay dominates the deactivation pathway.[21] The long lifetime arises from strong ligand-field stabilization and significant spin–orbit coupling at the Ru(II) center, which effectively suppresses non-radiative decay via thermally accessible metal-centered states.[22]

In contrast, compound 1 features a fundamentally different MLCT character, involving electron transfer from the Ru(II) center to a triphenylphosphine ligand. Unlike extended π-acceptor ligands such as bpy, PPh_3 offers limited π-conjugation and lacks efficient stabilization of the excited state. As a result, the MLCT state in compound 1 is more prone to nonradiative deactivation, particularly through charge separation and internal electron transfer processes. The presence of peripheral Cu(I) centers further contributes to excited-state quenching via redox-driven relaxation, as proposed in the sequential Ru(III)/PPh_3($\bullet^-$) to Cu(II)/PPh_3($\bullet^-$) electron transfer mechanism.

While $[Ru(bpy)_3]^{2+}$ exemplifies long-lived, emissive ^{3}MLCT states, compound 1 highlights how alterations in orbital composition and the presence of redox-active peripheral centers can drastically shorten excited-state lifetimes. These findings underscore the importance of tailored ligand and electronic design in controlling photophysical properties.

6. Conclusion

In this work, we have synthesized a novel heteronuclear Kuratowski complex, $[Ru^{II}Cu^{I}_4(Me_2bta)_6(PPh_3)_4]$, to investigate the influence of electron-rich Cu(I) centers on the electronic and photophysical properties of the system. CV reveals that Cu(I) oxidizes at significantly higher potentials than Ru(II), indicating that Cu(I) oxidation is less favorable. Notably, Cu(I) oxidation induces an irreversible Ru(II) oxidation, while bypassing the Cu(I) oxidation event allows for a reversible Ru(II/III) redox

Research Article
doi.org/10.1002/ejic.202500190

process. This behavior suggests coupled chemical processes during Cu(II) formation, likely involving ligand reorganization or structural rearrangement.

The UV–vis absorption spectrum exhibits a redshifted MLCT band compared to related Kuratowski complexes. In this system, the lowest-energy MLCT transition originates from Ru(II) to the PPh_3 ligands, rather than the more typical Ru(II) → benzotriazolate pathway. This unusual C-T direction, potentially overlapping with Cu(I) → benzotriazolate MLCT contributions, suggests subtle electronic interplay between the metal centers. However, time-resolved emission measurements reveal an ultrashort fluorescence lifetime at room temperature, indicating rapid nonradiative decay that prevents the formation of long-lived charge-separated states.

DFT and TD-DFT calculations support these findings. The HOMOs are localized on the Ru(II) center, while the LUMOs are predominantly situated on the PPh_3 ligands, yielding a computed HOMO–LUMO gap of 3.703 eV, consistent with the experimental absorption onset. The TD-DFT results confirm that the redshifted MLCT band arises from low-lying acceptor orbitals on PPh_3, rather than from direct Ru—Cu orbital interactions. This interpretation aligns with the electrochemical data, which reveal distinct, non-coupled redox events for Ru and Cu centers in the ground state.

Overall, this study highlights the delicate interplay between metal centers and ligand environments in modulating redox behavior, CT, and excited-state dynamics in polynuclear systems. Future studies could explore modifications to the ligand framework to stabilize the charge-separated state, potentially enabling longer-lived excited states for photochemical applications.

7. Experimental Section

All chemicals were purchased from commercial suppliers and used without further purification unless otherwise stated. Tetrabutylammonium chloride (95%, Apollo Scientific) and potassium tris(3,5-dimethylpyrazolyl)borate ([Tp*]K, > 98%, TCI) were used to synthesize $[NBu_4][Tp^*]$ via a metathesis reaction in anhydrous tetrahydrofuran ((THF, 99.8%, Thermo Scientific) under an argon atmosphere, following established literature procedures.[14] The copper precursor $[Cu(MeCN)_2(PPh_3)_2]$ was prepared according to published methods,[10] starting from copper(I) oxide (≥ 97%, Sigma-Aldrich), triphenylphosphine (PPh_3, 97%, Fluka), and anhydrous acetonitrile (≥ 99.8%, VWR). The ruthenium complex $[Ru(Me_2bta)_2(Me_2btaH)_4]$ was synthesized following a previously reported procedure.[7,23] Initially, $Ru(DMSO)_4Cl_2$ was prepared by reacting ruthenium(III) chloride (99.9%, Chempur) with dimethyl sulfoxide (DMSO, 99.5%, Sigma-Aldrich). This intermediate was then reacted with 5,6-dimethyl-1H-benzotriazole (99%, Acros Organics) to yield $[Ru(Me_2bta)_2(Me_2btaH)_4]$. Additional reagents included 2,6-lutidine (98%, Acros Organics), trichloromethane ($CHCl_3$, 99%, Alfa Aesar), diethyl ether (99%, Acros Organics), and ethanol (96%, VWR). All moisture- and air-sensitive manipulations were carried out under an inert argon atmosphere using standard Schlenk techniques.

FT-IR

FT-IR spectra were recorded using a Bruker Equinox 55 FT-IR spectrometer equipped with an attenuated total reflection unit, covering the spectral range of 4000–400 cm^{-1}. Signal intensities were denoted as strong (s), medium (m), or weak (w).

Raman Spectroscopy

Raman spectra were collected using a Thermo Scientific DXR Raman microscope with a 532 nm laser excitation source. The spectra were measured in the range of 3500–100 cm^{-1}.

TGA

TGA measurements were performed on a TA Instruments Q500 thermal analyzer under a nitrogen atmosphere from 25 to 800 °C, at a heating rate of 10 K min^{-1}. ICP-OES: Elemental composition was determined using a Varian Vista MPX instrument, calibrated with 10 ppm Ru and 20 ppm Cu standard solutions.

CHN

Microanalytical data were obtained using a Vario EL III elemental analyzer (Elementar Analysensysteme GmbH).

PXRD

Room-temperature PXRD patterns were recorded in the range of 4°–50° 2θ using a Seifert XRD 3003 TT diffractometer equipped with a Meteor1D detector and Cu $K\alpha_1$ radiation ($\lambda = 1.5406$ Å).

CV

Electrochemical measurements were conducted on a BioLogic SP-300 potentiostat in a three-electrode configuration using a 3 mm glassy carbon working electrode, a platinum wire counter electrode, and a pseudoreference electrode. Measurements were carried out in oxygen-free trichloromethane solutions under argon at room temperature with scan rates ranging from 200 to 10 mV s^{-1}.

UV–Vis Spectroscopy

Absorption spectra were recorded using a PerkinElmer Lambda 750s UV–vis–near infra red spectrometer in dual-beam mode over the 800–250 nm range.

Photoluminescence Spectroscopy

Steady-state fluorescence spectra were recorded on an Edinburgh Instruments FLS920 spectrometer equipped with double monochromators (excitation and emission), a thermoelectrically-cooled R928P photomultiplier tube detector, and a Xe900 continuous xenon lamp as excitation source.

Fluorescence Lifetime Measurements

Time-resolved emission measurements were performed using a Hamamatsu C5680 streak camera system coupled with a Princeton Instruments Acton SP2300i spectrograph. Excitation was achieved with an EKSPLA PT400 pulsed laser. All photophysical measurements were conducted at room temperature in standard quartz glass cuvettes (10 mm pathlength).

SCXRD

Crystals were selected directly from the mother liquor and mounted for diffraction analysis using a Bruker D8 Venture diffractometer equipped with a low-temperature device. Data were collected using monochromated Mo Kα radiation ($\lambda = 0.71073$ Å) from a sealed microfocus tube with a doubly curved silicon crystal monochromator.

Integration and absorption correction were carried out using Bruker SAINT and SADABS software (Apex3 v2019.1-0, SAINT V8.40 A, Bruker AXS Inc., Madison, WI, USA).[24] Structures were solved by direct methods using SHELXT 2014/5[25] and refined with SHELXL 2018/3.[26] All non-hydrogen atoms were refined anisotropically; hydrogen atoms were placed in calculated positions and refined using a riding model. Crystallographic data are provided in Table S1 of the Supporting Information, and full crystallographic information file (CIF) data have been deposited with the Cambridge Crystallographic Data Center (CCDC) under CCDC number 2425207 (for compound 1). These data can be obtained free of charge via the joint CCDC and FIZ Karlsruhe Access Structures service at www.ccdc.cam.ac./structuresuk or by using the direct DOI link: https://www.ccdc.cam.ac./services/structures?id=doi:10.1002/ejic.uk202500190.

DFT

All DFT calculations were performed using the TURBOMOLE program package (rev. V7-8-1).[27] Geometry optimizations were performed using the hybrid generalized gradient approximation functional B3-LYP (Becke, three-parameter, Lee–Yang–Parr) in combination with the def2-TZVP basis set,[18] employing Grimme's D4 dispersion correction.[19] Symmetry constraints were applied during optimization using the T, D_2, and S_4 point groups, with the S_4 configuration yielding the lowest energy. (Geometry optimizations under T_d point group symmetry constraints failed to converge and thus required to reducing the symmetry to point group D_2). Self-consistent field (SCF) convergence criteria were set to 10^{-6} Hartree, and the "m5" DFT integration grid was used for evaluating the exchange-correlation potential.

TD-DFT

TD-DFT calculations were performed using the random phase approximation method on the ground-state optimized geometries, employing the same functional, basis set, and dispersion correction. SCF convergence criteria were set to 10^{-6} Hartree and the "6" DFT integration grid was used for evaluating the exchange-correlation potential. 25 vertical singlet excitations were calculated to simulate the UV–vis absorption spectrum. The computed transitions were broadened and plotted for comparison with experimental data. Solvent effects were not included.

Synthesis: $[RuCu_4(Me_2bta)_6(PPh_3)_4]$ (1)

A solution of $[Cu(MeCN)_2(PPh_3)_2]$ (303 mg, 0.4 mmol) in degassed trichloromethane (7.0 mL) was added to a suspension of $[Ru(Me_2bta)_2(Me_2btaH)_4]$ (100 mg, 0.1 mmol) and 2,6-lutidine (46 μL, 0.40 mmol) in trichloromethane (7.0 mL) under argon atmosphere. The mixture was stirred at room temperature for 3 days, resulting in a clear yellow solution. Diethyl ether (15 mL) was added, and the solvent was slowly evaporated at room temperature, leading to large single crystals of compound 1. For better yield, the bulk product is washed with EtOH and purified using a short basic aluminum oxide column in trichloromethane, evaporation of the solvent results in a crystalline yellow product (164 mg, 0.072 mmol, 72%).

IR (cm^{-1}):3052 (w), 2966 (w), 2925 (w), 2890 (w), 2852 (w), 2366 (w), 2331 (w), 1479 (m), 1434 (s), 1373 (m), 1311 (w), 1290 (w), 1182 (w), 1147 (s), 1110 (m), 1091 (s), 1025 (m), 997 (s), 921 (w), 850 (s), 744 (s), 694 (s), 617 (w), 584 (w), 522 (s), 505 (s), 474 (m), and 428 (m).

Raman (cm^{-1}):1586 (w), 1573 (m), 1459 (w), 1374 (s), 1314 (w), 1191 (s), 1158 (s), 1097 (w), 1039 (s), 999 (s), 855 (w), 731 (w), 516 (w), 503 (m), 221 (w), and 120 (w).

CHN calc. for RuCu4P4C120H108N18: C 63.18, H 4.77, N 11.05; found: C 61.69, H 4.71, N 11.31

ICP-OES Ru/Cu ratio expected 1:4; measured 1:4.00

Acknowledgements

The authors gratefully acknowledge Binh Minh Nguyen and Wolfgang Brütting for performing the lifetime measurement. All authors are grateful for the financial support from the University of Augsburg.

Open Access funding enabled and organized by Projekt DEAL.

Conflict of Interest

The authors declare no conflict of interest.

Data Availability Statement

The CIF files are available from the CCDC under the deposition number(s) provided in the Experimental Section.

Keywords: benzotriazole · crystal structure · density functional theory · metal-to-ligand charge transfer · photophysics · ruthenium(II)

[1] S. Chen, K. Li, F. Zhao, L. Zhang, M. Pan, Y.-Z. Fan, J. Guo, J. Shi, C.-Y. Su, *Nat. Commun.* **2016**, *7*, 13169.
[2] S. Zhang, Q. Wang, L. M. Thierer, A. B. Weberg, M. R. Gau, P. J. Carroll, N. C. Tomson, *Inorg. Chem.* **2019**, *58*, 12234.
[3] a) D. Hayes, L. Kohler, R. G. Hadt, X. Zhang, C. Liu, K. L. Mulfort, L. X. Chen, *Chem. Sci.* **2018**, *9*, 860; b) X. Liu, D. Hayes, L. X. Chen, X. Li, *J. Phys. Chem. A* **2023**, *127*, 1831.
[4] Y.-Y. Liu, M. Grzywa, M. Tonigold, G. Sastre, T. Schüttrigkeit, N. S. Leeson, D. Volkmer, *Dalton Trans.* **2011**, *40*, 5926.
[5] a) H. Bunzen, M. Grzywa, A. Kalytta-Mewes, D. Volkmer, *Dalton Trans.* **2017**, *46*, 2618; b) R. Röß-Ohlenroth, C. Freudig, M. Kraft, H. Bunzen, D. Volkmer, *Cryst. Growth Des.* **2022**, *22*, 379.
[6] K. Knippen, D. Matuszczyk, M. Kraft, B. Bredenkötter, G. Eickerling, T. Lis, D. Volkmer, M. Stępień, *Chem. Eur. J.* **2022**, *28*, e202103480.
[7] W. G. Daul, M. Hirrle, B. Eisfeld, M. Kraft, H.-A. K. von Nidda, D. Volkmer, *Inorg. Chem.* **2024**, *63*, 5027.
[8] W. G. Rehfuß, A. Kalytta-Mewes, M. Kraft, B. M. Nguyen, W. Brütting, D. Volkmer, *Dalton Trans.* **2025**, *54*, 6910.
[9] S. Biswas, M. Tonigold, M. Speldrich, P. Kögerler, M. Weil, D. Volkmer, *Inorg. Chem.* **2010**, *49*, 7424.
[10] D. Li, R. Li, Z. Qi, X. Feng, J. Cai, X. Shi, *Inorg. Chem. Commun.* **2001**, *4*, 483.
[11] C. F. Macrae, I. Sovago, S. J. Cottrell, P. T. A. Galek, P. McCabe, E. Pidcock, M. Platings, G. P. Shields, J. S. Stevens, M. Towler, et al., *J. Appl. Crystallogr.* **2020**, *53*, 226.
[12] D. Denysenko, M. Grzywa, J. Jelic, K. Reuter, D. Volkmer, *Angew. Chem.* **2014**, *53*, 5832.
[13] G. Socrates, *Infrared and Raman Characteristic Group Frequencies. Tables and Charts*, John Wiley & Sons, Chichester **2001**.
[14] T. W. Werner, S. Reschke, H. Bunzen, H.-A. K. von Nidda, J. Deisenhofer, A. Loidl, D. Volkmer, *Inorg. Chem.* **2016**, *55*, 1053.
[15] M. Biner, H. B. Buergi, A. Ludi, C. Roehr, *J. Am. Chem. Soc.* **1992**, *114*, 5197.
[16] Z.-X. Yao, J.-Z. Li, H.-H. Wang, X. Cheng, L.-L. Hou, D.-N. Yu, D. Chen, W.-Y. Dan, K.-G. Liu, *Dalton Trans.* **2022**, *51*, 6053.
[17] H. V. R. Dias, H.-J. Kim, H.-L. Lu, K. Rajeshwar, N. R. de Tacconi, A. Derecskei-Kovacs, D. S. Marynick, *Organometallics* **1996**, *15*, 2994.
[18] A. D. Becke, *J. Chem. Phys.* **1993**, *98*, 5648.
[19] E. Caldeweyher, C. Bannwarth, S. Grimme, *J. Chem. Phys.* **2017**, *147*, 34112.

[20] S. Kümmel, *Adv. Energy Mater.* **2017**, *7*, 1700440.
[21] M. Chergui, *Acc. Chem. Res.* **2015**, *48*, 801.
[22] K. Kalyanasundaram, *Coord. Chem. Rev.* **1982**, *46*, 159.
[23] T. B. Rauchfuss *Inorganic Syntheses*, Wiley, Hoboken **2010**.
[24] L. Krause, R. Herbst-Irmer, G. M. Sheldrick, D. Stalke, *J. Appl. Crystallogr.* **2015**, *48*, 3.
[25] G. M. Sheldrick, *Acta Crystallogr., Sect. C: Struct. Chem.* **2015**, *71*, 3.
[26] G. M. Sheldrick, *Acta Crystallogr. A Found. Adv.* **2015**, *71*, 3.
[27] Y. J. Franzke, C. Holzer, J. H. Andersen, T. Begušić, F. Bruder, S. Coriani, F. Della Sala, E. Fabiano, D. A. Fedotov, S. Fürst, et al., *J. Chem. Theory Comput.* **2023**, *19*, 6859.

Manuscript received: April 10, 2025
Revised manuscript received: June 9, 2025
Version of record online: July 9, 2025